

# A 3D lattice Boltzmann – phase-field model of three-phase contact line dynamics on curved boundaries

M. Benioug<sup>a,b\*</sup>

<sup>a</sup>Analysis and Modeling for Environment and Health (UMR-AMES), Nouakchott, Mauritania

<sup>b</sup>Higher Institute of Industrial Engineering, Nouakchott, Mauritania

Received 2 December 2023; accepted 27 May 2025

---

## Abstract

In this paper, we present a three-dimensional multiphase fluid lattice Boltzmann model based on the phase-field theory. The conservative Allen-Cahn equation was used to describe the interface dynamics between two different fluids. The proposed model extends the model proposed in [Fakhari et al., Physical Review E 96 (2017) No. 053301] to three space dimensions and we show how to improve the accuracy of the model at high density ratios by computing gradients more accurately. We also propose an accurate method for implementing the three-phase contact angle on curved boundaries. Several benchmark test cases have been performed with realistic parameters for a water-air system to demonstrate the improvement in accuracy of our model, compared to existing methods. Specifically, flow in a cylindrical capillary has been simulated and the results have been compared to previous methods and analytical solutions.

© 2025 University of West Bohemia in Pilsen.

*Keywords:* lattice Boltzmann method, phase-field method, contact angle, multiphase fluid, contact line dynamics, curved boundary

---

## 1. Introduction

Multiphase fluid interactions are almost ubiquitous in natural and industrial processes, for example, in the food, pharmaceutical and personal care industries [3,6]. Some practical examples of multiphase fluid problems are polymer processing [17], enhanced oil recovery [4], microfluidics [16] and high-performance heat exchangers [8]. Among the two common modeling approaches—sharp-interface and diffuse-interface (phase-field) methods—the latter is widely favored for problems involving complex interface dynamics (coalescence, phase change, moving contact lines) due to its ability to naturally capture topology changes [33]. In recent years, the lattice Boltzmann method (LBM) has gained prominence as an efficient mesoscopic framework for simulating multiphase flows [23], owing to its simplicity in handling interfacial physics and excellent parallel scalability. Most multiphase LBM models fall into four main families [39]: color-gradient, pseudo-potential, free-energy, and phase-field approaches. Table 1 summarizes the key characteristics of these approaches, including their strengths, limitations, and typical capability for high-density-ratio flows.

Recent years have seen especially rapid development of phase-field LBM methods for multiphase flows. In this approach, the interface is evolved by a diffuse-interface equation (either Cahn-Hilliard or Allen-Cahn), coupled to the LBM solver for hydrodynamics. The Cahn-Hilliard formulation ensures global mass conservation but involves fourth-order spatial derivatives and may suffer droplet mass loss below a critical radius [43]. The Allen-Cahn formulation,

---

\*Corresponding author. Tel.: +46 738 422 929, e-mail: benioug@gmail.com.  
<https://doi.org/10.24132/acm.2025.881>

Table 1. Comparison of main multiphase LBM modeling approaches

<b>LBM approach</b>	<b>Key strengths</b>	<b>Key challenges</b>	<b>High-density ratio capability</b>
Color-gradient	<ul style="list-style-type: none"> <li>– Physically intuitive (“colored” fluids)</li> <li>– Captures interface morphology well</li> <li>– Suitable for moderate density/viscosity contrasts [28]</li> </ul>	<ul style="list-style-type: none"> <li>– Limited to low density ratios</li> <li>– Anisotropic surface tension</li> <li>– Pronounced spurious currents [21]</li> </ul>	<i>Low</i> (unstable at high density ratios) [2]
Pseudo-potential	<ul style="list-style-type: none"> <li>– Simple to implement (no explicit interface equation)</li> <li>– Effective for droplet/bubble dynamics</li> <li>– Widely used and validated [36]</li> </ul>	<ul style="list-style-type: none"> <li>– Thermodynamic inconsistency</li> <li>– Strong spurious currents</li> <li>– Limited stability at high density ratios [32]</li> </ul>	<i>Moderate</i> (improved with MRT schemes) [12]
Free-energy	<ul style="list-style-type: none"> <li>– Thermodynamically consistent</li> <li>– Explicit control over surface tension</li> <li>– Accurate interface representation [35]</li> </ul>	<ul style="list-style-type: none"> <li>– Requires solving Poisson’s equation</li> <li>– Computationally expensive</li> <li>– Early models lacked Galilean invariance [19]</li> </ul>	<i>Moderate</i> (possible but rarely used due to stiffness) [24]
Phase-field	<ul style="list-style-type: none"> <li>– Physically grounded (free energy-based)</li> <li>– Naturally captures moving contact lines</li> <li>– Conservative models support high density ratios [27]</li> </ul>	<ul style="list-style-type: none"> <li>– CH-type: small droplet loss</li> <li>– AC-type: may need mass correction</li> <li>– Requires parameter calibration [27]</li> </ul>	<i>High</i> (stable up to ~1000:1) [31]

in contrast, uses only second-order derivatives and is easier to implement locally, but originally allowed slight phase mass leakage [40]. To overcome this, conservative Allen-Cahn schemes introduce a Lagrange multiplier or modified forcing to strictly conserve mass [11]. This class of models has demonstrated improved stability for large density ratios [25, 31] and has been applied to complex interface phenomena including droplet coalescence, breakup, and dynamic wetting on flat surfaces [41]. However, handling three-phase contact line dynamics on curved solid boundaries (e.g., droplets in non-flat geometries) remains challenging. Only a few studies have begun to address wetting boundary conditions on curved surfaces using phase-field or related LBM models [1, 42], highlighting the need for further development in this area.

The aim of our work is to provide a stable and accurate phase-field lattice Boltzmann model for simulation of high density ratio flows (typically water-air systems) in complex geometries in 3D. In this study, we improve on existing conservative Allen-Cahn phase-field lattice Boltz-

mann models in two ways. First, we improve the accuracy of the velocity-based model by Fakhari et al. [10] for high density ratios by computing gradient terms more accurately. Second, we extend the model to three space dimensions, including proposing a method to implement boundary conditions for the conservative Allen-Cahn equation in 3D with different contact angles on general curved boundaries. The proposed model was evaluated on several test cases and compared to the previous momentum-based [9] and velocity-based [10] models.

## 2. Mathematical model

### 2.1. Phase-field equation

We introduce the phase-field  $\phi(t, \mathbf{x})$  for time  $t$  and space-variable  $\mathbf{x} = (x, y, z)$ , which attains the value zero in the light fluid and one in the heavy fluid. Following [11, 40], we let the evolution of the phase-field be determined by the equation

$$\frac{\partial \phi}{\partial t} + \nabla \cdot (\phi \mathbf{u}) = \nabla \cdot \left\{ M \left[ \nabla \phi - \frac{4}{\xi} \phi(1 - \phi) \frac{\nabla \phi}{|\nabla \phi|} \right] \right\}. \quad (1)$$

Mobility  $M$  represents the rate at which the interface between two fluids evolves under the influence of the chemical potential. It dictates how quickly the phase-field variable  $\phi$  adjusts to changes in the chemical potential gradient. Generally, the value of  $M$  should be chosen based on the balance between numerical stability and computational efficiency. The mobility  $M$  is often set to a small value (e.g., approximately 0.01 – 0.1) to ensure stability without excessively slowing down the simulation [44]. In (1),  $\mathbf{u}$  is the fluid velocity vector, and  $\xi$  is the interface thickness of the diffuse interface. The equation has the property that the right hand side becomes zero for the one-dimensional (1D) phase-field profile given by

$$\phi_0(\mathbf{x}) = \frac{1}{2} \left\{ 1 - \tanh \left[ 2 \frac{(\mathbf{x} - \mathbf{x}_0) \cdot \mathbf{v}}{\xi} \right] \right\}, \quad (2)$$

which therefore, represents a stationary solution to (1) with  $\mathbf{u} = 0$ , describing a flat interface located at  $x = x_0$  and perpendicular to the unit vector  $\mathbf{v}$  (which points from the heavy fluid to the light one).

Although (2) describes a one-dimensional equilibrium phase-field profile, it remains valid in three-dimensional simulations when interpreted along the local normal direction to the interface. In our model, this direction is given by the unit vector  $\mathbf{n} = \nabla \phi / |\nabla \phi|$ , allowing the 1D profile to be applied locally in any spatial dimension.

In the presence of solid boundaries, the boundary conditions for  $\phi$  are determined by the equilibrium contact angle  $\theta$ . The boundary condition used is

$$\frac{\partial \phi}{\partial \mathbf{n}} = \frac{4}{\xi} \phi(1 - \phi) \cos \theta, \quad (3)$$

where  $\mathbf{n}$  is the unit normal to the surface, directed outward from the fluid domain. The boundary condition can be derived from a free energy formulation [26], but it should also be noted that the equilibrium profile (2) satisfies this boundary condition exactly when the phase interface intersects a flat surface at an angle  $\theta$ , i.e., when  $\mathbf{v} \cdot \mathbf{n} = \cos \theta$ .

## 2.2. Navier-Stokes equations

The fluid velocity  $\mathbf{u}$  and the pressure  $p$  are determined by the incompressible Navier-Stokes equations for multi-phase flow

$$\nabla \cdot \mathbf{u} = 0, \quad (4)$$

$$\varrho(\phi) \left[ \frac{\partial \mathbf{u}}{\partial t} + (\mathbf{u} \cdot \nabla) \mathbf{u} \right] = -\nabla p + \nabla \cdot [\eta(\phi) (\nabla \mathbf{u} + (\nabla \mathbf{u})^T)] + \mu \nabla \phi + \mathbf{F}_b, \quad (5)$$

where  $\varrho(\phi) = \varrho_H \phi + \varrho_L (1 - \phi)$  is the local density and  $\eta(\phi) = \eta_H \phi + \eta_L (1 - \phi)$  is the local dynamic viscosity of the fluid. Here,  $\varrho_H$  and  $\varrho_L$  are the densities of the heavy and light fluid, respectively, and similarly for the viscosities  $\eta_H$  and  $\eta_L$ . The chemical potential  $\mu$  is given by

$$\mu[\phi] = \frac{3}{2} \frac{\sigma}{\xi} (8f'(\phi) - \xi^2 \Delta \phi) = \frac{3}{2} \frac{\sigma}{\xi} [16\phi(1 - \phi)(1 - 2\phi) - \xi^2 \Delta \phi]. \quad (6)$$

The coefficients are chosen so that the equilibrium profile (2) yields  $\mu[\phi_0] = 0$  and so that the surface tension  $\sigma$  equals the integral of the free energy density across the interface, i.e.,

$$\sigma = \int_{-\infty}^{\infty} E[\phi_0(\mathbf{x}_0 + t\mathbf{v})] dt, \quad (7)$$

where  $E[\phi] = \frac{12\sigma}{\xi} \phi^2 (1 - \phi)^2 + \frac{3}{4} \sigma \xi |\nabla \phi|^2$  is the total free energy density, and  $\mu[\phi] = \delta E / \delta \phi$ .

The surface tension force is chosen to be  $\mathbf{F}_s = \mu[\phi] \nabla \phi$  and  $\mathbf{F}_b$  is a body force, for example, a gravitational force. This formulation is the same as, e.g., in [9].

## 2.3. Lattice Boltzmann method

### 2.3.1. Lattice Boltzmann equations (LBE) for the phase-field equation

To solve the phase-field equation (1), we apply the method used in [9–11], but extended to three space dimensions. Equation (1) is an advection-diffusion equation with an added non-linear flux term, and the method is, therefore, rather straightforward although the non-linear term requires some attention.

Given a velocity set  $\{\mathbf{e}_q\}_{q=0}^{Q-1}$  and corresponding distribution function  $\{f_q\}_{q=0}^{Q-1}$ , the lattice Boltzmann equation (LBE) using a single relaxation time collision is given by

$$f_q(\mathbf{x} + \mathbf{e}_q, t + 1) = f_q(\mathbf{x}, t) + \frac{1}{\tau_\phi} (f_q^{\text{eq}}(\mathbf{x}, t) - f_q(\mathbf{x}, t)), \quad (8)$$

where  $\tau_\phi$  is the relaxation time for the phase-field LBE and we use the time-step  $\Delta t = 1$ . The equilibrium distribution is given by

$$f_q^{\text{eq}} = \phi \Gamma_q + w_q c_s^{-2} M \left[ \frac{4}{\xi} \phi (1 - \phi) \right] \mathbf{e}_q \cdot \frac{\nabla \phi}{|\nabla \phi| + \varepsilon}, \quad (9)$$

where

$$\Gamma_q = w_q \left[ 1 + \frac{\mathbf{e}_q \cdot \mathbf{u}}{c_s^2} + \frac{(\mathbf{e}_q \cdot \mathbf{u})^2}{2c_s^4} - \frac{\mathbf{u} \cdot \mathbf{u}}{2c_s^2} \right], \quad (10)$$

$c_s$  is the speed of sound in the system, and  $w_q$  denotes the equilibrium weights associated with the LB model. The mobility  $M$  is given by the relaxation time as

$$M = c_s^2 \left( \tau_\phi - \frac{1}{2} \right) \quad (11)$$

and  $\varepsilon = 10^{-16}$  is a small number to avoid division by zero. The value of the phase-field  $\phi$  is computed as

$$\phi = \sum_{q=0}^{Q-1} f_q. \quad (12)$$

In this work, we use the D3Q19 LB model with  $Q = 19$  velocities and corresponding weights  $w_q$  as given in [7], with  $c_s = 1/\sqrt{3}$ . Equation (8) is solved using a standard collision-streaming scheme.

The computation of the gradient  $\nabla\phi$  is discussed in Section 2.3.3.

### 2.3.2. LBE for the hydrodynamic equations

To solve the Navier-Stokes equations (4)–(5), we adopt a velocity-based lattice Boltzmann method (LBM) originally proposed by Zu and He [45], which was further enhanced by Fakhari et al. [10]. This method improves the representation of incompressibility and momentum conservation, especially for multiphase flows with large density and viscosity contrasts.

*Momentum-based model* [9]:

In traditional momentum-based LB models, the distribution function  $f_\alpha$  is designed so that its first moment yields the momentum  $\rho\mathbf{u}$ . These models typically require solving for pressure and velocity simultaneously, and often suffer from challenges in numerical stability and efficiency at high density ratios. They also frequently employ force coupling techniques (e.g., Guo forcing scheme) and necessitate predictor-corrector steps.

*Velocity-based model* [10,45]:

In contrast, the velocity-based model defines a modified distribution function  $g_\alpha$ , whose first moment directly recovers the macroscopic velocity  $\mathbf{u}$  (by normalizing with density  $\rho$ ). This decouples pressure from velocity, simplifies the collision operator (especially in multiple relaxation time schemes), and significantly improves numerical stability. Fakhari et al. [10] introduced further enhancements including:

- a conservative phase-field model for interface tracking,
- simplified nonlocal dependencies (only phase-field is nonlocal),
- avoidance of biased difference schemes, ensuring mass and momentum conservation.

*Extension introduced in this work:*

Building on this framework, we further enhance the model by adding forcing terms, see (14), to recover the correct pressure and viscous stress components. Our approach also integrates additional correction terms to ensure that the pressure and stress tensors in the macroscopic Navier-Stokes equations are accurately reproduced. Specifically, by scaling the distribution function  $g$  with  $\rho$ , the velocity becomes the first moment rather than momentum – this eliminates the need for density normalization post-processing and facilitates handling of incompressible regimes more accurately. This improved formulation, thus, bridges the benefits of velocity-based approaches with a more physically consistent force incorporation scheme, enabling robust simulations of complex multiphase systems with curved boundaries and high contrast in material properties.

Here, we present a scheme using a single relaxation time (SRT) model for the collision operator, but in Appendix A, the method is extended to a multiple relaxation time (MRT) model for improved accuracy and stability. The SRT model was used except where noted below.

The lattice Boltzmann equation for hydrodynamics is, thus, assuming  $\Delta t = 1$ ,

$$\bar{g}_q(\mathbf{x} + \mathbf{e}_q, t + 1) = \bar{g}_q(\mathbf{x}, t) + \frac{1}{\tau}(\bar{g}_q^{\text{eq}}(\mathbf{x}, t) - \bar{g}_q(\mathbf{x}, t)) + F_q(\mathbf{x}, t), \quad (13)$$

where  $\bar{g}_q$  is the modified distribution function,  $\tau$  is the local relaxation time, and the forcing term is

$$F_q = w_q \frac{\mathbf{e}_q \cdot \mathbf{F}}{\rho c_s^2}. \quad (14)$$

The modified equilibrium distribution function is

$$\bar{g}_q^{\text{eq}} = g_q^{\text{eq}} - \frac{1}{2}F_q \quad \text{and} \quad g_q^{\text{eq}} = p^* w_q + (\Gamma_q - w_q), \quad (15)$$

where  $p^* = p/\rho c_s^2$  is the normalized pressure. The local fluid density  $\rho$  is computed using the phase-field as

$$\rho = \phi \rho_H + (1 - \phi) \rho_L, \quad (16)$$

where  $\rho_H$  and  $\rho_L$  are the densities of the heavy and light fluid, respectively.

As remarked in [10], the implementation of the forcing term (14) is accurate to leading order, while Guo et al. [15] and He et al. [18] give more accurate forcing schemes. However, as in [10], we have also compared our results to results using higher-order forcing schemes and noticed no difference.

For the velocity-based scheme, two additional force terms,  $\mathbf{F}_p$  and  $\mathbf{F}_\eta$ , are added in order to achieve correct pressure and viscous forces [45]. The total force is, therefore,

$$\mathbf{F} = \mathbf{F}_s + \mathbf{F}_b + \mathbf{F}_p + \mathbf{F}_\eta, \quad (17)$$

where

$$\mathbf{F}_p = -p^* c_s^2 \nabla \rho, \quad \mathbf{F}_\eta = \nu (\nabla \mathbf{u} + (\nabla \mathbf{u})^T) \cdot \nabla \rho. \quad (18)$$

The viscous force is implemented as in [10] as

$$F_{\eta,i} = -\frac{\nu}{\tau c_s^2} \sum_{j=1}^d \left[ \sum_{q=1}^Q e_{qi} e_{qj} (\bar{g}_q - g_q^{\text{eq}}) \right] \frac{\partial \rho}{\partial x_j}, \quad (19)$$

where we note that the density gradient is computed according to (16) as

$$\nabla \rho = (\rho_H - \rho_L) \nabla \phi. \quad (20)$$

The relaxation time  $\tau$  is related to the local kinematic viscosity as

$$\nu = c_s^2 \left( \tau - \frac{1}{2} \right) \quad (21)$$

and is determined locally by linear interpolation of the dynamic viscosity  $\eta = \rho \nu$  as

$$\eta(\phi) = \phi \eta_H + (1 - \phi) \eta_L, \quad (22)$$

and then using (21) to compute  $\tau$ . In Section 3.5, we also compare different methods to interpolate and compute  $\tau$ .

The hydrodynamic velocity and scaled pressure are calculated as

$$p^* = \sum_{q=0}^{Q-1} \bar{g}_q, \quad \mathbf{u} = \sum_{q=1}^{Q-1} \bar{g}_q \mathbf{e}_q + \frac{\mathbf{F}}{2\varrho}, \quad (23)$$

where the pressure is computed first and used in the computation of  $\mathbf{F}$ .

### 2.3.3. Computation of gradients

The gradient  $\nabla\phi$  in (9) and (20) is generally computed by an isotropic central finite difference scheme (see, e.g., [22])

$$\nabla\phi(\mathbf{x}, t) \approx \frac{1}{2c_s^2} \sum_{q=1}^{Q-1} w_q \mathbf{e}_q (\phi(\mathbf{x} + \mathbf{e}_q, t) - \phi(\mathbf{x} - \mathbf{e}_q, t)). \quad (24)$$

However, when using the velocity-based approach for high density ratios, there is a problem with this scheme to compute gradients. This is because the correct computation of the pressure term in (5) depends on the cancellation of two terms, namely (after dividing the equation with  $\varrho$ )

$$-\frac{1}{\varrho} \nabla p = -\frac{1}{\varrho} \nabla(\varrho c_s^2 p^*) = -\frac{p^* c_s^2 \nabla \varrho}{\varrho} - c_s^2 \nabla p^*, \quad (25)$$

where the first term is  $\mathbf{F}_p/\varrho$ , which is the actual pressure force added to the scheme by (14), and the second stems from the lattice Boltzmann scheme, see [45]. A similar situation holds for the viscous force term (18)<sub>2</sub>. It is therefore important that the vector  $\nabla\varrho/\varrho$  is computed accurately. When using (24) to compute this quantity,  $\nabla\phi$  is multiplied with  $(\varrho_H - \varrho_L)/\varrho$ , which is large where  $\varrho$  is small, which is the case in the light phase if the density ratio is high (regardless of the value chosen for  $\varrho_H$ ). Any numerical errors in the finite difference scheme (24) are therefore amplified. In Fig. 1, the errors in  $\nabla\varrho/\varrho$  across the phase interface at a density ratio of 1 000 are clearly seen.

We therefore propose to instead use the fact that  $\nabla \log \varrho = \nabla\varrho/\varrho$  and use the scheme

$$\frac{\nabla\varrho}{\varrho}(\mathbf{x}, t) \approx \frac{1}{2c_s^2} \sum_{q=1}^{Q-1} w_q \mathbf{e}_q [\log \varrho(\mathbf{x} + \mathbf{e}_q, t) - \log \varrho(\mathbf{x} - \mathbf{e}_q, t)]. \quad (26)$$

From Fig. 1, it is obvious that this approach improves the accuracy significantly. The difference in maximum error is almost an order of magnitude. The gradient of the phase-field, needed in (9) can then be computed as

$$\nabla\phi = \frac{\varrho}{\varrho_H - \varrho_L} \nabla \log \varrho. \quad (27)$$

Clearly, this equation can not be used if the density ratio is 1, and  $\varrho_H = \varrho_L$ , but then the common gradient scheme (24) is accurate and should be used instead.

The Laplacian of the phase field is also needed in order to compute the chemical potential (6) and can be computed from the relation

$$\Delta \log \varrho = \nabla \cdot \left( \frac{\nabla \varrho}{\varrho} \right) = \frac{\Delta \varrho}{\varrho} - \frac{|\nabla \varrho|^2}{\varrho^2} \quad (28)$$

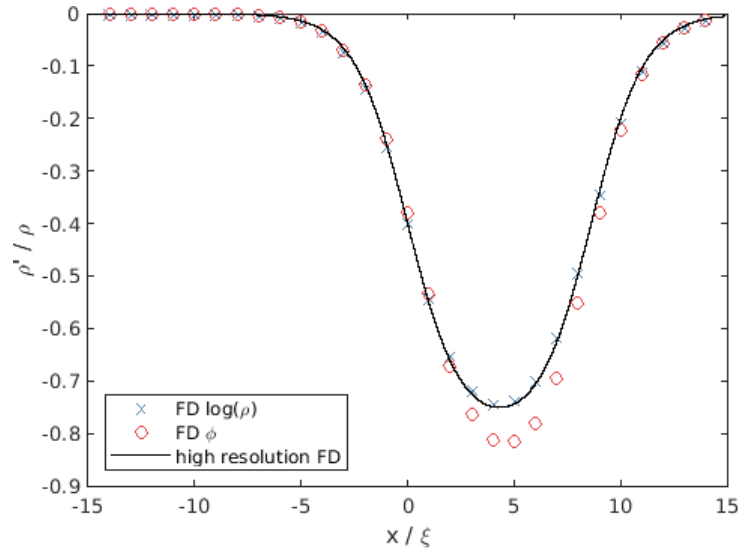


Fig. 1. The values for  $\rho'/\rho$ , where  $\rho' \equiv \nabla \rho$ , computed for the equilibrium profile (2) with a density ratio of  $\rho_H/\rho_L = 1000$  and interface width  $\xi = 5$ , using finite differences of  $\log \rho$  (marked as "x", equation (26)) and the phase-field  $\phi$  (marked as "o", equation (24)). The solid line shows values computed with a high-resolution finite difference scheme

and of course,  $\Delta \rho = (\rho_H - \rho_L)\Delta \phi$ . The Laplacian  $\Delta \log \rho$  is computed using isotropic finite differences as [22]

$$\Delta \log \rho(\mathbf{x}, t) \approx \frac{1}{c_s^2} \sum_{q=1}^{Q-1} w_q \mathbf{e}_q [\log \rho(\mathbf{x} + \mathbf{e}_q, t) - 2 \log \rho(\mathbf{x}, t) + \log \rho(\mathbf{x} - \mathbf{e}_q, t)]. \quad (29)$$

Note that both finite difference formulas, (26) and (29), may be simplified to loop over only half the velocities and to evaluate the central value only once, for speedup.

This optimization leverages the symmetry of the lattice directions (e.g.,  $\mathbf{e}_q$  and  $-\mathbf{e}_q$ ) to reduce redundant computations. Each pair of opposite directions contributes symmetrically to the gradient or Laplacian, allowing the loop to run over half the stencil without loss of accuracy.

The quantity  $\log \rho$  can therefore be chosen as the non-local quantity instead of  $\phi$  for the purpose of computing gradients. However, the value of  $\phi$  may still need to be saved as an auxiliary scalar for the purpose of implementing boundary conditions for the phase-field equation (see Section 2.4). It should also be noted that computing the logarithm is a rather costly operation and will affect the computational efficiency of the scheme. We have not performed a study of this, as it will be implementation dependent, but we see a reduction in the number of lattice updates per second by around 10% when using the logarithm-based gradient, for a not very optimized code.

#### 2.3.4. Interpolation of viscosity

The choice of interpolation method for the phase-field dependent viscosity  $\eta(\phi)$  is of major importance for the accuracy of the numerical scheme, especially at high density ratios. This is because the surface tension force  $\mathbf{F}_s$  is significant only in the transition region between the phases, which is also where the viscosity changes. Additionally, in the LBM setting, the dynamic viscosity  $\eta$  is determined through the kinematic viscosity, which is in turn related to

the relaxation time  $\tau$  through (21), which determines the stability of the simulation. Thus, the relation

$$\eta(\phi) = \varrho(\phi)c_s^2 \left( \tau(\phi) - \frac{1}{2} \right) \quad (30)$$

relates the interpolation schemes for  $\eta$ ,  $\varrho$  and  $\tau$ . It is obvious here why the density ratio influences the interpolation accuracy.

The natural choice for interpolation of  $\varrho$  is the linear interpolation (16) and we have not considered other interpolation schemes. However, for the interpolation of  $\eta$ , several choices are possible, in addition to the linear interpolation (22), which is our default choice. To get high accuracy across the interface, a sharp jump in  $\eta$  may be considered, given by

$$\eta(\phi) = \begin{cases} \eta_H & \phi \geq 0.5, \\ \eta_L & \phi < 0.5. \end{cases} \quad (31)$$

However, this has the disadvantage of being unstable in many cases due to the sharp gradients. Another possible scheme is the harmonic interpolation of  $\eta$ ,

$$\eta(\phi) = \left[ \frac{1}{\eta_H} \phi + \frac{1}{\eta_L} (1 - \phi) \right]^{-1}, \quad (32)$$

which favors low viscosity values.

Through (30), it is also possible to instead interpolate the relaxation time  $\tau$ , as has been done in the literature, see, e.g., [22, 25]. One approach is to use a linear interpolation of the relaxation time

$$\tau = \phi\tau_H + (1 - \phi)\tau_L, \quad (33)$$

while another approach is to use a harmonic interpolation of kinematic viscosity, which amounts to

$$\frac{1}{\tau - \frac{1}{2}} = \frac{\phi}{\tau_H - \frac{1}{2}} + \frac{1 - \phi}{\tau_L - \frac{1}{2}}. \quad (34)$$

While the effect of different choices have been discussed previously [10, 22, 25], all these choices have not been compared for high density ratios. In Fig. 2, we therefore plot the resulting dynamic viscosity and relaxation time for different interpolations, at density ratio 1000 and dynamic viscosity ratio 100, which is close to a water-air system. The effects on accuracy in certain test cases is discussed in Sections 3.3 and 3.5.

It is clear from Fig. 2a that the linear interpolation of  $\tau$ , see (33), creates a region of artificial high viscosity across the interface. The harmonic interpolation of  $\tau$ , see (34), does the same, although less notably so, while harmonic interpolation of  $\eta$  results in lower viscosity over a wide range. On the other hand, Fig. 2c shows that sharp and harmonic  $\eta$  interpolations (31) and (32) result in very low values for  $\tau$  at the interface (minimum value about 0.501 and 0.502, respectively), which may cause stability problems.

#### 2.4. Boundary conditions

For the hydrodynamic equations, we use simple bounce-back boundary conditions to implement no-slip boundary conditions on the boundaries. It would be straight-forward to implement any other standard boundary-conditions with higher accuracy, see, e.g., [14, 30]. Although this would lead to consistent localization of the boundary in the hydrodynamic and phase-field equations, which is desirable, it is not likely to influence the results presented here appreciably.

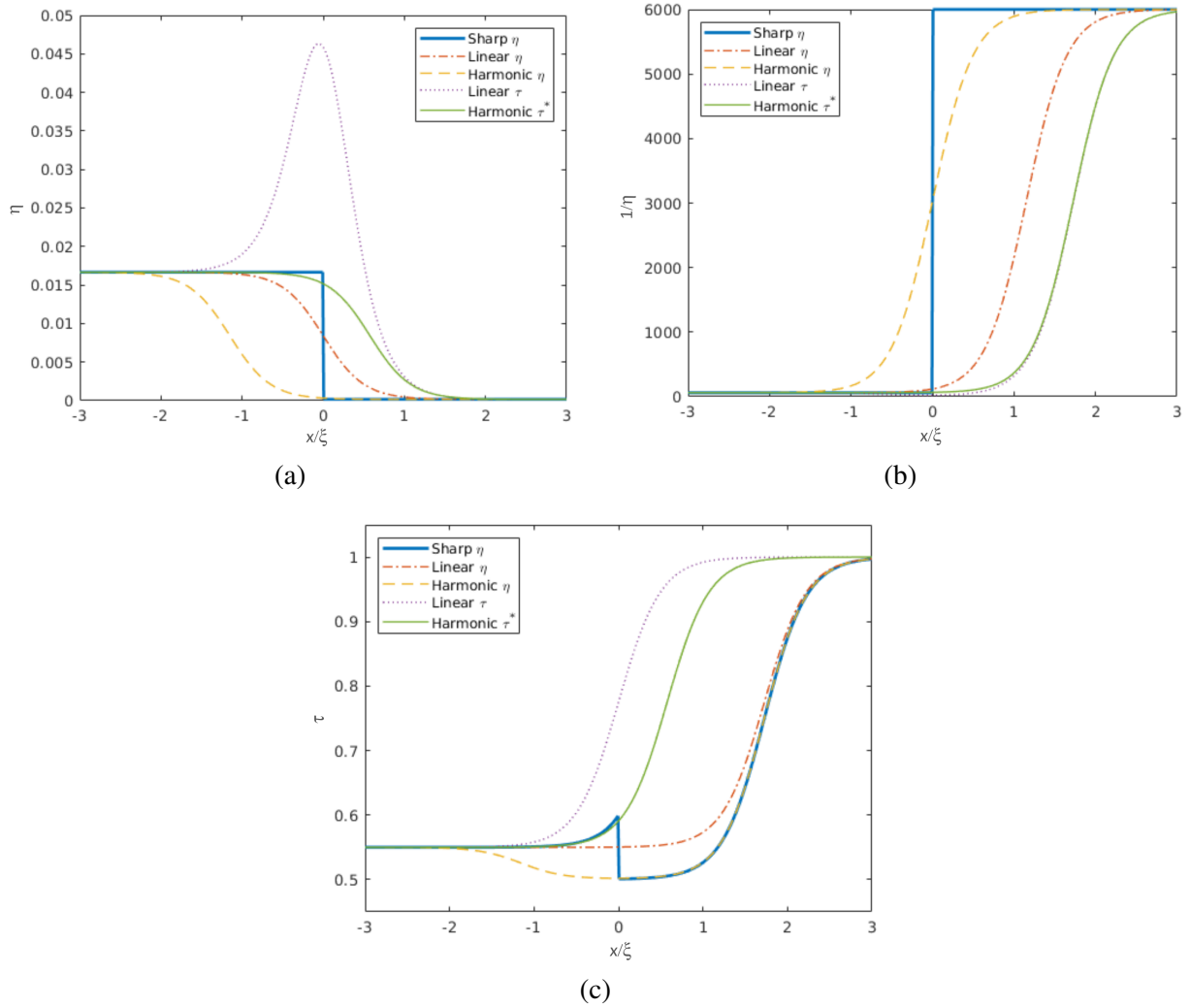


Fig. 2. (a) Dynamic viscosity  $\eta(\phi)$ , (b) reciprocal of dynamic viscosity  $1/\eta(\phi)$ , and (c) relaxation time  $\tau$  across the phase interface assuming the equilibrium profile (9) using the different interpolation schemes: equation (31) (thick solid), equation (21) (dashed), equation (32) (dash-dotted), equation (33) (dotted), and equation (34) (solid). The  $x$ -axis represents the distance along the normal direction to the interface

For the phase-field equation, we need to implement the boundary condition (3), which is a non-linear Robin-type boundary condition. The scheme is different from the one used by Fakhari and Bolster [9] for the Allen-Cahn equation in 2D in that a central difference is always used across the boundary to derive the boundary scheme and that there is an explicit equation for the unknown quantity.

The problem, as always for lattice Boltzmann boundary conditions, is to assign proper values to the incoming populations coming from a lattice node located just outside the domain. In Fig. 3, these nodes are marked as "o" and we refer to them as ghost nodes. In addition, the boundary conditions need to supply values for the computation of the gradient and Laplacian of the phase field across the boundary, which are computed by finite differences using (26) and (29), respectively.

In order to preserve mass exactly, we use half-way bounce-back boundary conditions for the incoming populations, i.e.,

$$f_q^*(\mathbf{x}_g) = f_q^*(\mathbf{x}_f), \quad (35)$$

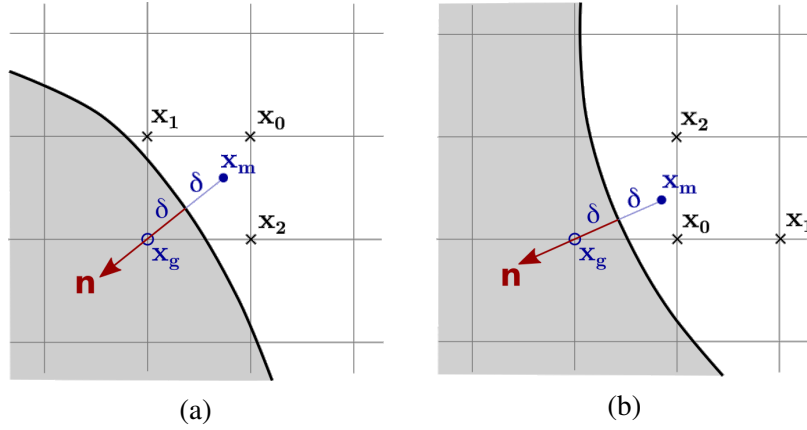


Fig. 3. Two examples of boundary configurations, shown in 2D for clarity. In (a), values in grid nodes can be interpolated to the mirror point  $\mathbf{x}_m$ , while in (b), extrapolation is required as the interpolation nodes would need to be outside the domain. One of the ghost nodes is denoted  $\mathbf{x}_g$  and is marked with an empty circle. The corresponding mirror point, at a distance  $2\delta$  from  $\mathbf{x}_g$ , is marked with a filled circle, and the grid nodes used for interpolation/extrapolation are marked with crosses

where the lattice velocity  $c_q$  intersects the boundary from the ghost node  $\mathbf{x}_g$ ,  $c_{\bar{q}}$  is the opposite grid velocity,  $\mathbf{x}_f = \mathbf{x}_g + c_q$  and  $f^*$  is the post-collision distribution. It should be noted that while for the diffusion equation, bounce-back conditions are inaccurate since they force not only a zero normal flux but also a zero tangential flux [13], this is not a major issue here because the flux is

$$\mathbf{j} = M \left[ \nabla\phi - \frac{4}{\xi}\phi(1-\phi)\frac{\nabla\phi}{|\nabla\phi|} \right] \quad (36)$$

and is identically zero for the equilibrium profile (2).

However, to compute the finite differences correctly, an accurate value of the phase field  $\phi$  must be computed at the ghost node, using the boundary condition. Using the outward unit normal  $\mathbf{n}$ , the mirror image of the ghost node  $\mathbf{x}_g$  can be computed as

$$\mathbf{x}_m = \mathbf{x}_g - 2\delta\mathbf{n},$$

where  $\delta$  is the distance from the ghost node to the boundary along the normal direction. The normal derivative in (3) is now approximated by a central finite difference as

$$\left. \frac{\partial\phi}{\partial\mathbf{n}} \right|_{\mathbf{x}=\mathbf{x}_b} \approx \frac{\phi(\mathbf{x}_g) - \phi(\mathbf{x}_m)}{2\delta}, \quad (37)$$

which is second order accurate. The right hand side of (3) is evaluated at  $\phi = \phi(\mathbf{x}_b) \approx (\phi(\mathbf{x}_g) + \phi(\mathbf{x}_m))/2$ . Using these approximations yields a quadratic equation for  $\phi(\mathbf{x}_g)$  with the solution

$$\phi(\mathbf{x}_g) = \frac{1}{a} \left[ a - 1 + \sqrt{(a-1)^2 + 4a\phi(\mathbf{x}_m)} \right] - \phi(\mathbf{x}_m), \quad (38)$$

where  $a = 4\delta/\xi$ .

All that now remains is to correctly estimate the value of  $\phi$  at the mirror point  $\mathbf{x}_m$ , which is done by interpolation. We can use four lattice nodes in a "tripod" (three in 2D) for linear interpolation, as indicated in Fig. 3. We label these  $\mathbf{x}_0$  and  $\mathbf{x}_i = \mathbf{x}_0 + s_i\mathbf{e}_i$ ,  $i = 1, \dots, d$ , where  $s_i \in \{-1, 1\}$ , depending on the orientation of the "tripod" and  $d$  is the number of dimensions.

The node  $\mathbf{x}_0$  is chosen as the fluid node closest to  $\mathbf{x}_m$  and the  $\mathbf{x}_i$  are chosen as close as possible to  $\mathbf{x}_m$ . The problem is that in some configurations, such as in Fig. 3b, we need to extrapolate to get the value at the mirror point, which may cause instabilities because the extrapolated value of  $\phi$  may be below 0. To circumvent this, we use an additional quadratic term in the interpolation polynomial, which becomes

$$h(\mathbf{x}) = \alpha_0 + \sum_{i=1}^d \alpha_i (\mathbf{x} - \mathbf{x}_0)_i + \alpha_n [\mathbf{n} \cdot (\mathbf{x} - \mathbf{x}_0)]^2. \quad (39)$$

As an extra condition to determine the coefficient  $\alpha_n$ , we use the boundary condition (3), in the linearized form

$$\partial_n h(\mathbf{x}_b) = G(h(\mathbf{x}_b)) \approx G(h(\mathbf{x}_0)) + G'(h(\mathbf{x}_0))(h(\mathbf{x}_b) - h(\mathbf{x}_0)), \quad (40)$$

where in our case  $G(\phi) = \frac{4}{\xi}\phi(1 - \phi)$ . Inserting the polynomial (39) into the condition (40) and using the natural interpolation conditions  $h(\mathbf{x}_i) = \phi(\mathbf{x}_i)$ ,  $i = 0, \dots, d$ , we can solve for the coefficients to get

$$\alpha_0 = \phi(\mathbf{x}_0), \quad (41)$$

$$\alpha_n = \frac{G(\alpha_0) - \sum_{i=1}^d s_i (\phi(\mathbf{x}_i) - \phi(\mathbf{x}_0)) v_i}{(2 - G'(\alpha_0) \mathbf{n} \cdot \hat{\mathbf{x}}_b) (\mathbf{n} \cdot \hat{\mathbf{x}}_b) - \sum_{i=1}^d s_i n_i^2 v_i}, \quad (42)$$

$$\alpha_k = s_k (\phi(\mathbf{x}_k) - \phi(\mathbf{x}_0)) - s_k \alpha_n n_k^2 \quad (43)$$

for  $k = 1, \dots, d$ , where we have set  $\hat{\mathbf{x}}_b = \mathbf{x}_b - \mathbf{x}_0$  and  $\mathbf{v} = \mathbf{n} - G'(\alpha_0) \hat{\mathbf{x}}_b$ .

### 3. Numerical results

To illustrate and evaluate the accuracy and applicability of our model, several numerical tests were performed. Unless otherwise noted, parameters corresponding to a water-air system at 20° C were used, namely  $\rho_H/\rho_L = 831$  and  $\eta_H/\eta_L = 55$ . The mobility was  $M = 0.02$  in all cases. The value  $M = 0.02$  was chosen to have a compromise between guaranteeing numerical stability and obtaining a reasonable speed of evolution of the interface. This value guarantees that the interface evolves neither too fast (which could cause instability) nor too slowly (which would be inefficient) corresponding to the relaxation time  $\tau_\phi = 0.56$ , and the interface width was chosen to be  $\xi = 5$ . The parameters  $\rho_H = 1$  and  $\tau_L = 1.0$  were used (with  $\tau_H$  computed from the density ratio), and the surface tension was set to  $\sigma = 10^{-3}$  unless otherwise stated. Note that the surface tension parameter used in the simulations is dimensionless and defined in lattice units. Its physical counterpart can be recovered via the conversion relation  $\sigma = C_\rho C_L^3 / C_t^2 \tilde{\sigma}$ , as detailed in Appendix B. For reference, the typical surface tension between water and air under ambient conditions is  $\tilde{\sigma} = 0.072 \text{ N m}^{-1}$ .

Below, we first examine the volume preservation and accuracy of boundary conditions by comparing to analytical steady-state solutions for droplets on a flat surface and a sphere. Then, the accuracy of the present method is compared to previous velocity-based [10] and momentum-based [9] methods for layered flows and a stationary meniscus in a cylindrical capillary. Finally, the dynamics of capillary flows in a cylindrical capillary is studied.

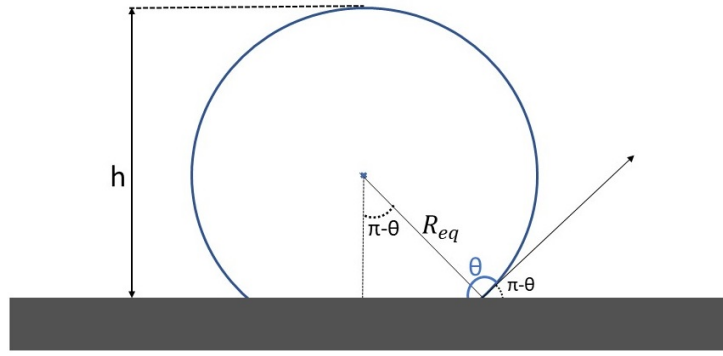


Fig. 4. The contact angle  $\theta$  between a droplet and a flat surface as well as the height  $h$  and equilibrium radius  $R = R_{eq}$  of the droplet

### 3.1. Case 1: Droplet on a flat surface

In this test case, a spherical droplet was placed on top of a flat surface with an initial contact angle of  $90^\circ$ , while the contact angle  $\theta$  was set to a different value. The droplet then instantly moves to balance the system by minimizing its energy to the solid-air, solid-liquid and liquid-air interfaces. This is mainly achieved by minimizing the surfaces between the liquid and the other phases, while keeping the correct contact angle. This state is reached when the forces acting on the triple line solid-liquid-air are in equilibrium. In the absence of gravity, the only mobilizing factor is interfacial tension. A computational domain  $220 \times 220 \times 100$  was used. The initial radius of the droplet, on a neutrally wetting surface was  $R_0 = 40$  in lattice units. Periodic boundary conditions were imposed in the  $x$ - and  $y$ -directions and a symmetry condition was imposed in the  $z$ -direction. The bounce-back method was used to satisfy the no-slip boundary condition at the wall solid surface and the boundary conditions described in Section 2.4 were applied for the phase field.

In order to validate the numerical accuracy of our model, a comparison was made to the analytical relationship between the contact angle  $\theta$  and the height  $h$ , Fig. 4.

Consider the droplet shown in Fig. 5a. To minimize its surface energy, the droplet adopts a shape of a spherical cap (since no gravitation is present), which can be seen as part of a sphere of radius  $R$ , which is intersected by a plane. The height of the droplet is  $h = R - R \cos \theta$ . The initial droplet is a half sphere, and thus, its volume is

$$V_0 = \frac{2}{3} \pi R_0^3. \quad (44)$$

To determine  $R$ , a relation is needed to link the volume  $V$  of the spherical cap, the contact angle  $\theta$  and  $R$ , namely

$$V = \pi \int_{R-h}^R (R^2 - x^2) dx = \dots = \pi \left( hR^2 - \frac{h^3}{3} \right) = \frac{\pi}{3} R^3 (2 - 3 \cos \theta + \cos^3 \theta). \quad (45)$$

Assuming the volume of the droplet is conserved, the radius  $R$  can be expressed in terms of the volume  $V = V_0$  and the angle  $\theta$  as

$$R = \left[ \frac{V_0}{\frac{\pi}{3} (2 - 3 \cos \theta + \cos^3 \theta)} \right]^{\frac{1}{3}} = \left( \frac{2}{2 - 3 \cos \theta + \cos^3 \theta} \right)^{\frac{1}{3}} R_0. \quad (46)$$

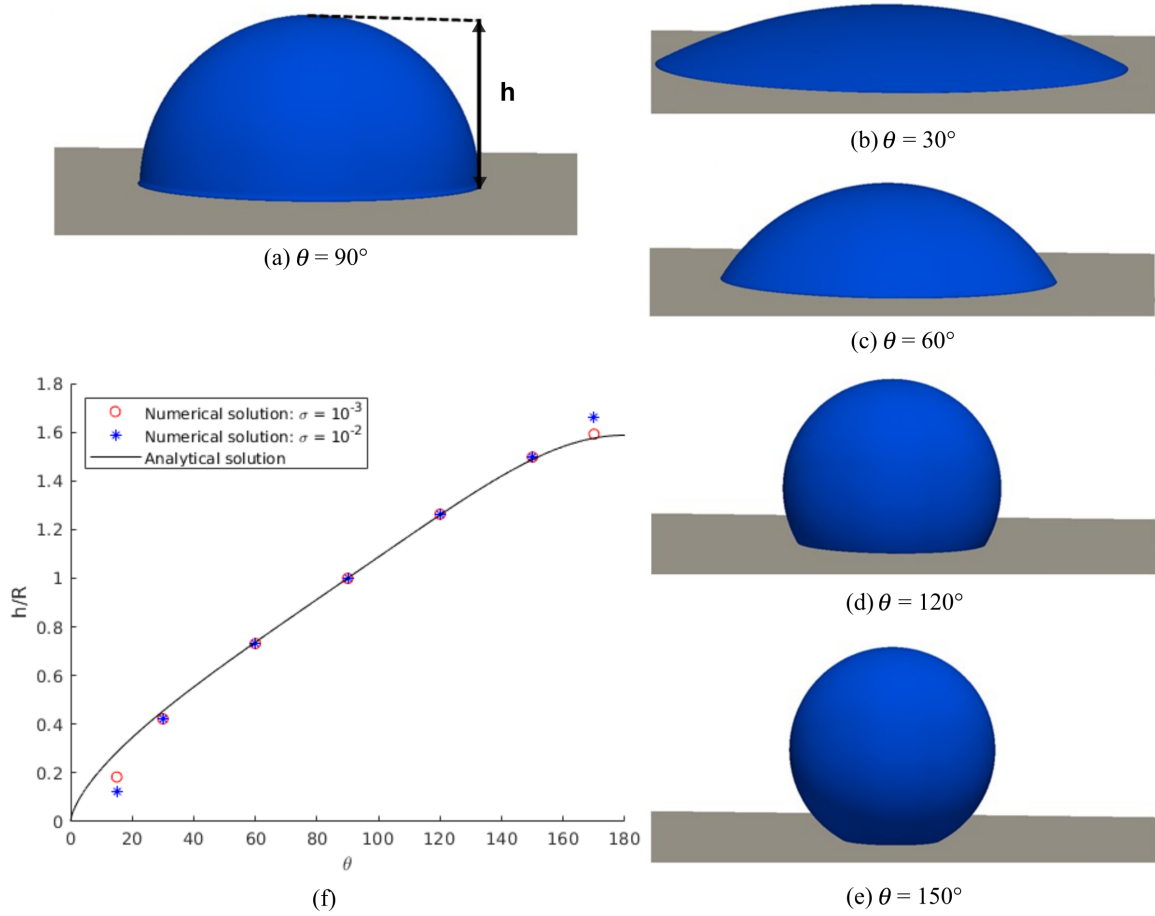


Fig. 5. (a) Initial position of the droplet, (b) at  $\theta = 30^\circ$ , (c) at  $\theta = 60^\circ$ , (d) at  $\theta = 120^\circ$ , (e) at  $\theta = 150^\circ$ , (f) comparison between numerical and analytic relationships

Computations were performed at several contact angles as shown in Fig. 5b–e. Fig. 5e shows a good agreement between the numerical results and the analytical solution for a large range of contact angles from  $15^\circ$  to  $170^\circ$ . The results are almost identical for both values of the surface tension coefficient  $\sigma = 10^{-3}$  and  $\sigma = 10^{-2}$  except for the extreme values  $15^\circ$  and  $170^\circ$  where the results are more precise for  $\sigma = 10^{-3}$ . The maximum error is at  $\theta = 15^\circ$ , where the relative error is about 35% for  $\sigma = 10^{-3}$ . At  $\theta = 30^\circ$ , however, the relative error is down to about 3%. In the rest of the simulations, we use the value  $\sigma = 10^{-3}$ .

### 3.2. Case 2: Droplet on a spherical surface

In this test case, the accuracy of our model was investigated on a curved surface by placing a droplet on a solid sphere. The computational domain was  $[0, L] \times [0, L] \times [0, 2L]$ . The center of the solid sphere, which had a radius  $R_s = 0.3L$ , was located at  $(L/2, L/2, L/2)$  and the droplet initially formed a sphere with radius  $R_0 = R_s$  centered at  $(L/2, L/2, L/2 + R_s)$ . This means the initial contact angle was  $60^\circ$ . If a different contact angle  $\theta$  is chosen for the boundary condition, the droplet will move on the solid surface and stop when it reaches the state of thermodynamic equilibrium. In its final state, the droplet can be represented as shown in Fig. 6. We assume that the droplet is axisymmetric and we neglect the effects of external forces, such as gravity.

Since the droplet volume is conserved, the final radius  $R$  of the droplet changes as the contact angle  $\theta$  on the spherical substrate is altered. For a given spherical substrate with radius

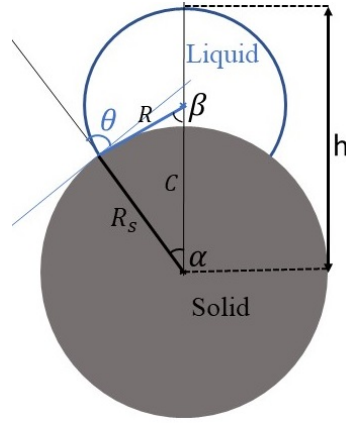


Fig. 6. Schematic illustration of the contact angle between a droplet and a solid sphere

$R_s$ , the volume  $V$  of the droplet having a contact angle  $\theta$  and a radius  $R$  is given by

$$V = \frac{1}{3}\pi R^3 (2 + 3 \cos \beta - \cos^3 \beta) - \frac{1}{3}\pi R_s^3 (2 - 3 \cos \alpha + \cos^3 \alpha), \quad (47)$$

where from the geometric relations shown in Fig. 6, we have  $\cos \alpha = R_s^2 + c^2 - R^2 / (2R_s c)$ ,  $R_s \sin \alpha = R \sin \beta$ , and  $\cos \beta = R^2 + c^2 - R_s^2 / (2Rc)$  with  $c = \sqrt{R^2 + R_s^2 - R_s R \cos \theta}$  and  $\beta + \theta_0 = \pi$ . By substituting the geometric relations into (4), the final droplet radius  $R$  can be determined as a function of the droplet volume  $V$  and  $\theta$ . First, the mesh dependency of our numerical results was investigated. Three alternative meshes were considered for this purpose  $L = 50, 100$ , and  $200$ . Periodic conditions were introduced at the boundaries in  $x$ - and  $y$ -directions. The results after reaching a steady state are illustrated in Fig. 7 for two contact angles, corresponding to a hydrophilic ( $\theta = 30^\circ$ ) and a hydrophobic ( $\theta = 150^\circ$ ) surface. As Fig. 7 shows, we can see that the interface of the droplet is almost identical for meshes  $100 \times 100 \times 200$  and  $200 \times 200 \times 400$ . Therefore, we use the  $100 \times 100 \times 200$  mesh for the rest of the simulations in this section. This choice is validated by the mesh convergence study in Fig. 8, which involved the use of five mesh configurations of the type  $N_x \times N_x \times 2N_x$ , where  $N_x$  takes the values  $50, 100, 150, 200$ , and  $250$ . The process entailed calculating the droplet height for each mesh to ensure the accuracy and stability of the simulation. By analyzing the

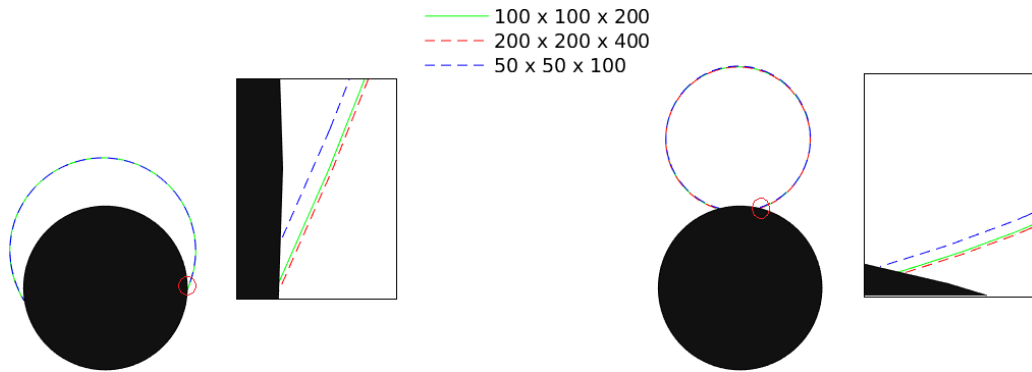


Fig. 7. Grid independence of the results for a droplet on a spherical surface solid. Comparison between three resolutions for cross-sections through the center of the domain:  $50 \times 50 \times 100$  (blue curve),  $100 \times 100 \times 200$  (green curve), and  $200 \times 200 \times 400$  (red curve) with  $\theta = 30^\circ$  (left) and  $\theta = 150^\circ$  (right)

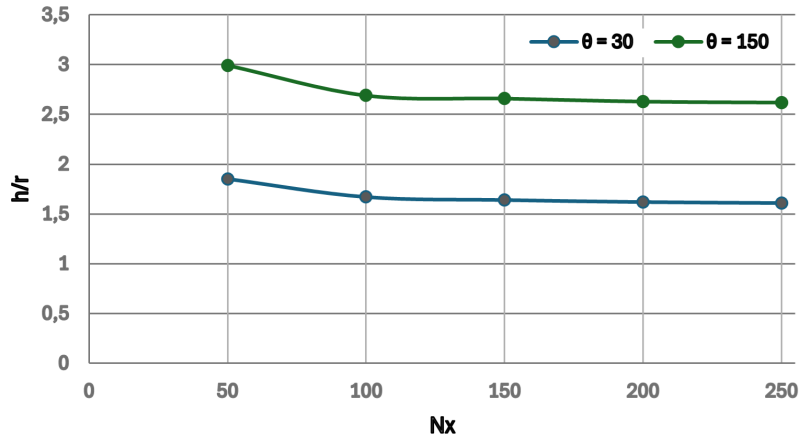


Fig. 8. Grid independence of the results for a droplet on a spherical surface solid. Comparison between five mesh at two contact angles  $\theta = 30^\circ$  and  $\theta = 150^\circ$

results, the appropriate mesh size was selected based on its ability to capture the droplet height with minimal computational error and sufficient precision.

Fig. 9 shows results for several different contact angles. A comparison between the numerical and analytical values of the maximum height of the droplet was made. The maximum height of the droplet  $h$  is the distance between the top of the droplet and the center of the solid sphere as shown in Fig. 6,  $h = c + R$ . The wetting/dewetting of the droplet was simulated at seven different surface conditions ranging from hydrophilic to hydrophobic with contact angles values from  $15^\circ$  to  $150^\circ$ , as shown in Fig. 9a–e.

Fig. 9f shows the dimensionless value of the droplet height  $h/R_s$  depending on the contact angle. These results show a good agreement with the analytical solution. The maximum error is at  $\theta = 30^\circ$ , and it is about 3 %, though at  $\theta = 15^\circ$  the contact line shows evidence of distortion and local errors.

### 3.3. Case 3: Layered Poiseuille flow between parallel plates

The region between two parallel plates,  $y \in [0, L]$ , was divided equally between the heavy and light fluids by setting  $\phi(y) = \phi_0(y - L/2)$ , according to (2) (with  $v = \hat{y}$ ). This results in the heavy fluid occupying the lower half of the channel ( $y \in [0, L/2]$ ) and the light fluid occupying the upper half ( $y \in [L/2, L]$ ). This setup corresponds to a classical gravity-driven two-phase Poiseuille flow configuration, commonly used to assess the accuracy of multiphase lattice Boltzmann models.

A body force was applied in the  $x$ -direction to drive the flow between the plates and periodic boundary conditions were applied in the  $x$ - and  $z$ -directions. The simulations were run in a  $2(L + 1) \times (L + 1) \times (L + 1)$  domain, with  $L = 84$  and bounce-back boundary conditions were applied on the parallel plates (the contact angle is not important here). Two options were investigated for the body force: 1)  $\mathbf{F}_b = F_0 \hat{x}$ , with  $F_0 = 5 \times 10^{-8}$ , similar to [25], and 2)  $\mathbf{F}_b = \rho(\phi) F_0 \hat{x}$  with  $F_0 = 10^{-6}$ , similar to [10]. The density ratio is here  $\rho_H/\rho_L = 1000$  and the viscosity ratio is  $\eta_H/\eta_L = 100$  to enable direct comparison with these references.

The velocity profiles for the first case are shown in Fig. 10. The numerical results using the present method are compared to the velocity-based method from [10] and the moment-based method from [9] as well as the analytical solution with a sharp change in dynamic viscosity, see [25], and a reference high-resolution finite difference solution using the linear interpolation

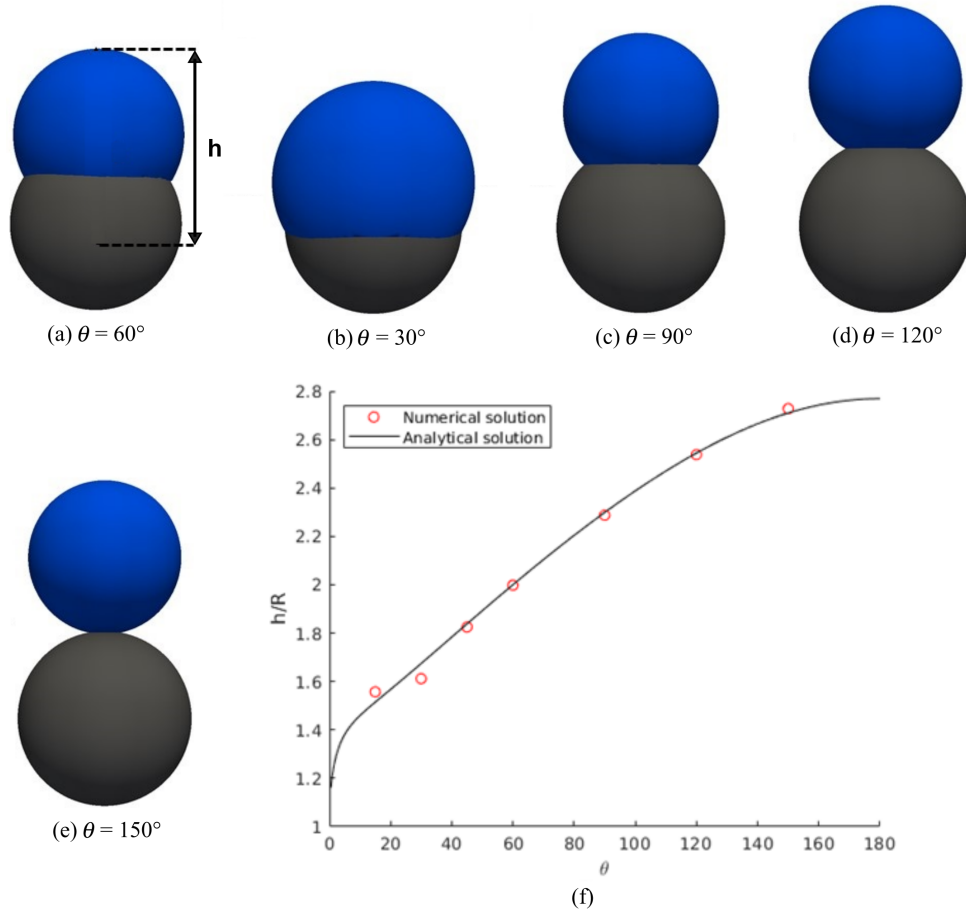


Fig. 9. The final position of a droplet on a spherical surface for different contact angles: (a) initial position of the droplet with  $\theta = 60^\circ$ , (b) with  $\theta = 30^\circ$ , (c) with  $\theta = 90^\circ$ , (d) with  $\theta = 120^\circ$ , (e) with  $\theta = 150^\circ$ , (f) comparison between numerical and analytical values for the relative height  $h/R$ , defined as shown in (a)

of  $\eta$  in (22). It is clear that the interpolation of the viscosity in the interface region has major impact on the solution. In order to understand the results, it is useful to note that the analytical solution for the velocity is

$$u_x(y) = \int_0^y \frac{C - F_0 \hat{y}}{\eta(\phi(\hat{y}))} d\hat{y}, \quad (48)$$

where  $C$  is an integration constant determined by the boundary conditions. Without computing the integral, it is easy to see that the value of  $1/\eta$  will determine the velocity profile. In Fig. 2b, it is seen that when using linear interpolation of viscosity, the value of  $1/\eta$  is too low in a wide part of the low viscosity region. This is the cause of the deviation from the analytical solution in Fig. 10. This can be partly remedied by using harmonic interpolation of  $\eta$ , which results in more accurate results in Fig. 10, but using MRT collisions (see Appendix A) due to stability problems with the low  $\tau$  seen in Fig. 2c. The most accurate results are of course obtained with a sharp interpolation, but as noted above, this causes stability problems.

In the region of light fluid it is clear that the present method performs better than the other LB methods, while in the heavy fluid the moment-based method agrees best with the finite difference solution. The present method performs better than the velocity-based method in both

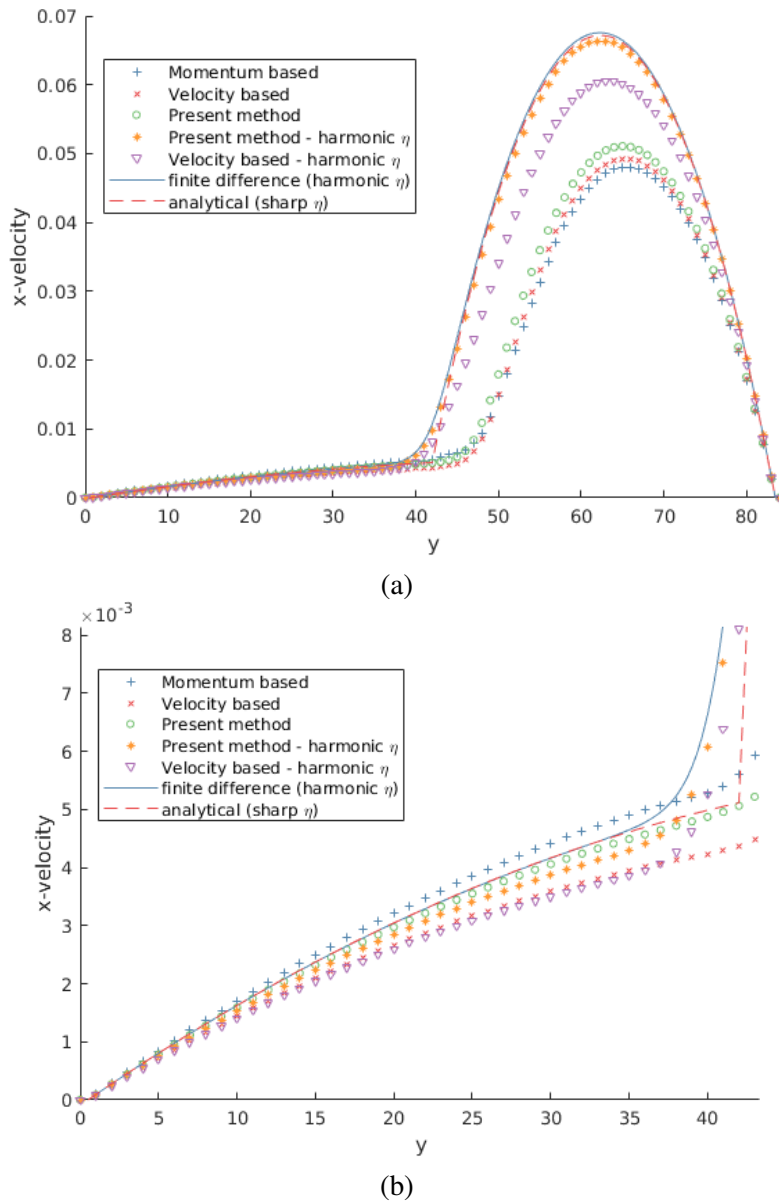


Fig. 10. Velocity profiles for flow between parallel plates driven by a constant body force  $\mathbf{F}_b = F_0 \hat{x}$ , with density ratio 1000 and viscosity ratio 100. The heavy fluid is on the left of the domain and the light fluid on the right. The numerical results for the present and previous methods, using linear (21) and harmonic (32) interpolation of viscosity, are compared to the analytical solution found in [25], using a sharp jump in dynamic viscosity, (dashed) and a high resolution finite difference solution using harmonic interpolation of viscosity (solid line). The whole domain is shown in the top figure, showing accuracy in the light phase, while the bottom figure is zoomed in on the heavy fluid region. All profiles correspond to the steady-state solution, after the velocity field has fully developed

regions, showing the importance of the improved accuracy in the gradient computations. The present method agrees well with the analytical solution in the heavy fluid, but it is unclear if this is a coincidence.

The velocity profiles for the second case with a density-dependent force are shown in Fig. 11 and are compared to a high-resolution finite difference solution using linear interpolation of density and dynamic viscosity. As was also noted by Fakhari et al. [10], the moment-based

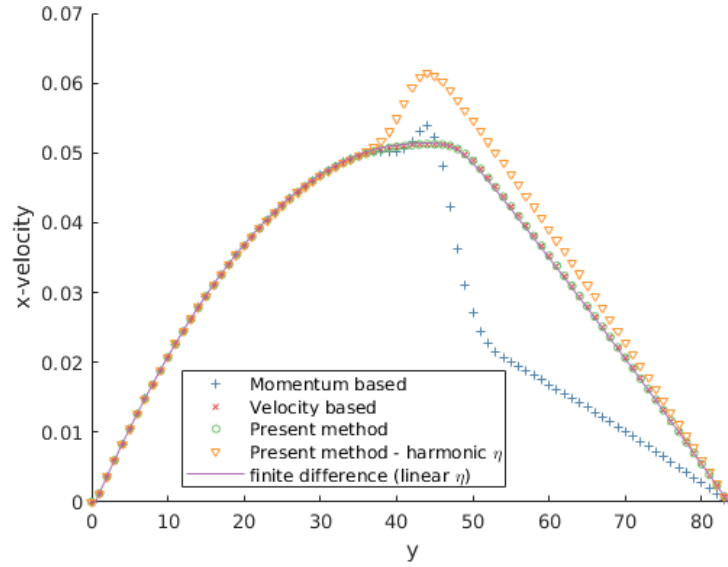


Fig. 11. Velocity profiles for flow between parallel plates driven by a force proportional to the density (like for example a gravitational force). The results from the lattice Boltzmann methods are compared to a high-resolution finite difference solution. All results use the linear interpolation of viscosity (21), except where the harmonic interpolation (32) is used (triangles). The fluid with high density and viscosity is on the left. The density ratio is 1 000 and the viscosity ratio is 100

method computes an erroneous solution in the heavy fluid and in the interface region. The present method and the velocity-based method [10] produce very similar results, which are very close to the finite difference solution. Note that using the harmonic interpolation (32) results in a bump in the solution due to mismatch between density and viscosity in the transition region.

In Fig. 12, the results of a convergence study for the two forcing cases are shown. The number of grid points  $N$  was varied while keeping the Cahn number  $Cn = \xi/N$  constant. For case 1 with constant force, the harmonic viscosity interpolation (32) and  $Cn = 5/42$  were used with an MRT scheme with  $\tau_l = 2.0$  (to avoid instabilities due to low values of  $\tau$  in the transition region). For case 2, the linear interpolation (21) and  $Cn = 4/42$  were used with the SRT scheme with  $\tau_l = 1.0$ . The density ratio was 1 000 and the viscosity ratio 100. The resulting velocities  $u_x$  were compared to a very high resolution finite difference solution  $u_x^{FD}$  and the relative  $L_2$ -norm of the error was computed as

$$\|\delta u\|_2 = \frac{\sqrt{\sum_{i=1}^N (u_x(y_i) - u_x^{FD}(y_i))^2}}{\sqrt{\sum_{i=1}^N (u_x^{FD}(y_i))^2}}. \quad (49)$$

The present method using the gradient computations in Section 2.3.3 was compared to the original velocity based method by Fakhari et al. [10]. The results show second-order convergence in all cases (contrary to the results in [10]), but with significantly lower errors for the present method (by a factor of 15 and 6, respectively, for the two cases). This shows the importance of the logarithm-based gradient computations to improve the accuracy at high density ratios.

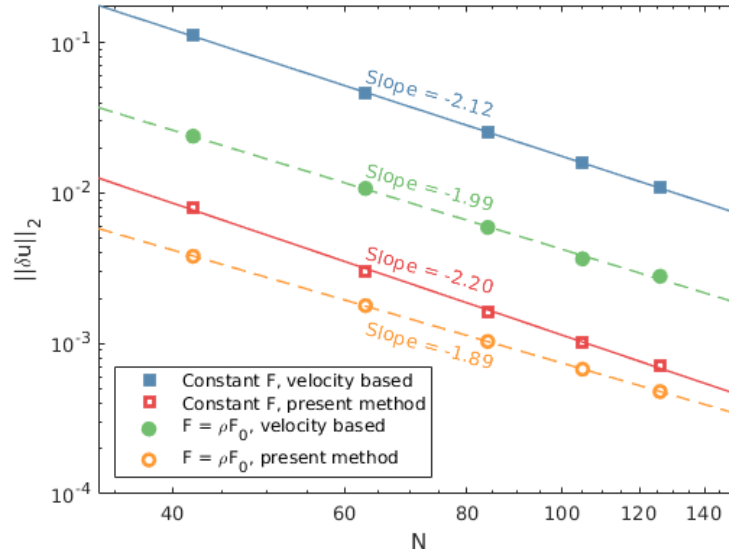


Fig. 12. Convergence study for the flows between parallel plates with a constant force (squares, solid lines) and density-dependent force  $\mathbf{F} = \varrho(\phi)\mathbf{F}_0$  (circles, dashed lines), at density ratio 1000 and viscosity ratio 100. Results for the present scheme, using the gradient computations in Section 2.3.3, (hollow markers) are compared to the original velocity-based scheme (filled markers). Lines are fits in log-log-scale with indicated slopes. See text for more details

### 3.4. Case 4: Stationary meniscus in a cylindrical capillary

Next, we investigate the equilibrium shape of a capillary meniscus in a cylindrical tube. The meniscus at the liquid front adopts a curved shape due to the contact angle  $\theta = 30^\circ$ , resulting in a pressure difference across the meniscus according to the Young-Laplace relation

$$\Delta p_c = \frac{2\sigma \cos \theta}{R}, \quad (50)$$

where  $\sigma$  is the surface tension (here,  $\sigma = 0.001$ ) and  $R = 15$  is the radius of the cylinder. In order to make the meniscus stationary, a counter-acting body force  $F_b = -\Delta p_c/L$  was applied, where  $L = 100$  is the length of the cylinder. A constant pressure,  $p = 0$ , was applied at both ends together with boundary conditions  $\phi = 1$  and  $\phi = 0$  at the left and right ends of the cylinder. To correctly simulate, this system requires accurate boundary conditions to get the correct spherical shape of the meniscus, in combination with a correct computation of the chemical potential and pressure gradient. An incorrect pressure drop or capillary force will cause the interface to drift with time, and thus, this test case is an overall indication of the accuracy of the simulation of capillary flows.

In Fig. 13a and 13b, the stationary pressure profiles and velocity profiles along a line through the center of the cylinder are shown, respectively. The pressure profiles are compared to an analytical profile with a slope given by  $F_b$  and a jump across the meniscus given by (50). The momentum-based method produces the best results, with a very low spurious velocity, while the velocity-based method deviates strongly in the pressure gradient in the heavy fluid, which causes a high spurious velocity and makes the meniscus move with time, which is seen by that the location of the pressure jump is to the right of the other profiles. The present method improves the situation through a more accurate computation of forces, resulting in a more accurate pressure profile and much lower spurious velocity, although the moment-based method is still

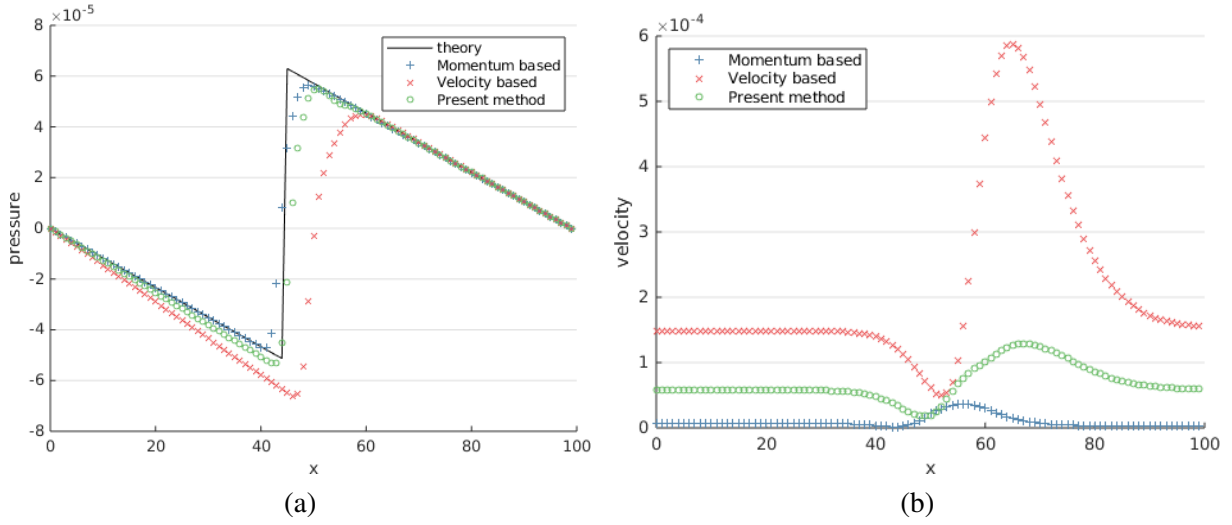


Fig. 13. Results for the simulation of a stationary meniscus in a cylindrical capillary: (a) the pressure profiles along a line through the center of the cylinder, compared to the pressure profile computed with a slope given by the body force  $F_b$  and a jump across the meniscus given by the Young-Laplace relation (50), and (b) the  $x$ -velocity profiles along the same center line (ideally, they should all be zero)

more accurate. Note that for all methods, there are local vortices formed close to the meniscus, which cause the peaks in the velocity profiles along the center line.

What is not seen very clearly in the figure is that the moment-based method yields a different average velocity in the light phase compared to the heavy phase, thus violating the incompressibility condition (4). The velocity-based methods on the contrary yield similar velocities in the two phases, except for a region close to the interface. This effect is also seen in dynamic simulations.

### 3.5. Case 5: Capillary flow in a cylinder

Capillary rise of a liquid into circular cylindrical capillaries is a standard and widely studied problem with very well documented experimental results [34,38]. Nevertheless, there are many challenges for the correct simulation of this system, including dynamic contact angles dependent on boundary conditions and velocity, initial effects, etc. The Poiseuille law expresses the balance between viscous forces and capillary and hydrostatic forces (neglected inertial effects), resulting in the equation

$$\frac{4}{R} [\eta_l h + \eta_g (L - h)] \frac{dh}{dt} = \sigma \cos(\theta) \quad (51)$$

for the height  $h$  reached by the liquid front at time  $t$ .  $L$  is the height of the cylinder,  $R$  is the radius of the cylinder,  $\eta_l$  is the liquid viscosity,  $\eta_g$  the gas viscosity,  $\sigma$  is the surface tension, and  $\theta$  is the equilibrium contact angle. If the viscosity of the gas is neglected, integration of (51) leads to the well-known Washburn's equation

$$h(t)^2 - h_0^2 = \frac{\sigma R \cos(\theta)}{2\eta_l} t \quad (52)$$

with the initial height  $h_0 = h(t = 0)$ . In our case, with the viscosity ratio 55 and a rather short cylinder, the gas viscosity can be safely neglected.

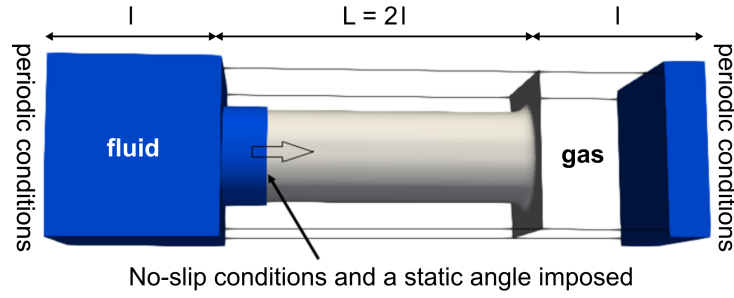


Fig. 14. Geometrical set-up of the simulation. The 3D geometry is divided into three parts. The left and right parts colored blue are filled by liquid and in the middle there is initially gas. The left and right part has periodic boundary conditions at all sides. In the middle, there is the true capillary cylinder: The boundary conditions are those of a solid wall with a given contact angle. Periodic boundary conditions are also imposed at the inlet and outlet sides.

The experimental results do not correspond to those found by (52). This difference is due to the assumption that the meniscus is spherical in shape and that the contact angle remains constant during fluid penetration into the tube. Several experimental studies have been performed to improve the prediction of the displacement of the liquid interface. All these studies show a change in the contact angle during the process of displacement due to a change in the velocity of the meniscus [5, 20, 34] and with a very different value compared to the static angle.

To validate the accuracy of our model, a comparison was made with the velocity-based method [10] and the momentum-based method [9], as well as with (52). The geometry used is depicted in Fig. 14. The computational domain was  $[0, 4l] \times [0, l] \times [0, l]$ , where  $l = 50$ . A horizontal cylindrical capillary of radius  $R = 0.3l$  was centered at  $x = 50$ ,  $y = l/2$ ,  $z = l/2$  with height  $L = 2l$ . Initially, the region between  $x = 64$  and  $x = 188$  was filled with gas and the rest was filled with fluid. At the walls of the capillary cylinder, no-slip boundary conditions and a given static contact angle were imposed. Outside the cylinder, periodic boundary conditions were imposed at the top, bottom and lateral surfaces in order to mimic an infinite reservoir. Periodic boundary conditions were also imposed at the inlet and outlet to ensure total conservation of mass inside the system.

Measurements of the meniscus dynamic contact angle were made by using the approach from Siebold et al. [37]. In their experimental study, the authors assumed that the meniscus was a portion of sphere and used the following equation to compute the contact angle:

$$\theta_d = \frac{\pi}{2} - 2 \arctan \left( \frac{2x_m}{d} \right). \quad (53)$$

Here,  $x_m$  is the height and  $d$  is the diameter of the meniscus ( $d = 2R$ ). This method was used to compute the dynamic contact angle from our numerical results.

Fig. 15a–c show the height  $h$  reached by the liquid front as a function of time. The present method is compared with the velocity based and the momentum based methods for a range of different equilibrium contact angles  $\theta_d$ . The solid straight line shows the profile of the theoretical solution (52), for a value of  $\theta$  equals to the final value of  $\theta_d$  calculated by (53). We can see a good agreement with the theoretical results for all methods, for all the contact angles, at late times. Many studies [29, 38] have reported that at the start of the wicking process, it takes time to form the meniscus in a capillary tube and the inertial effects are important. Here, the simulation is started with a flat surface, so the Washburn equation (52) is valid only after some time. This may explain the deviations at early times.

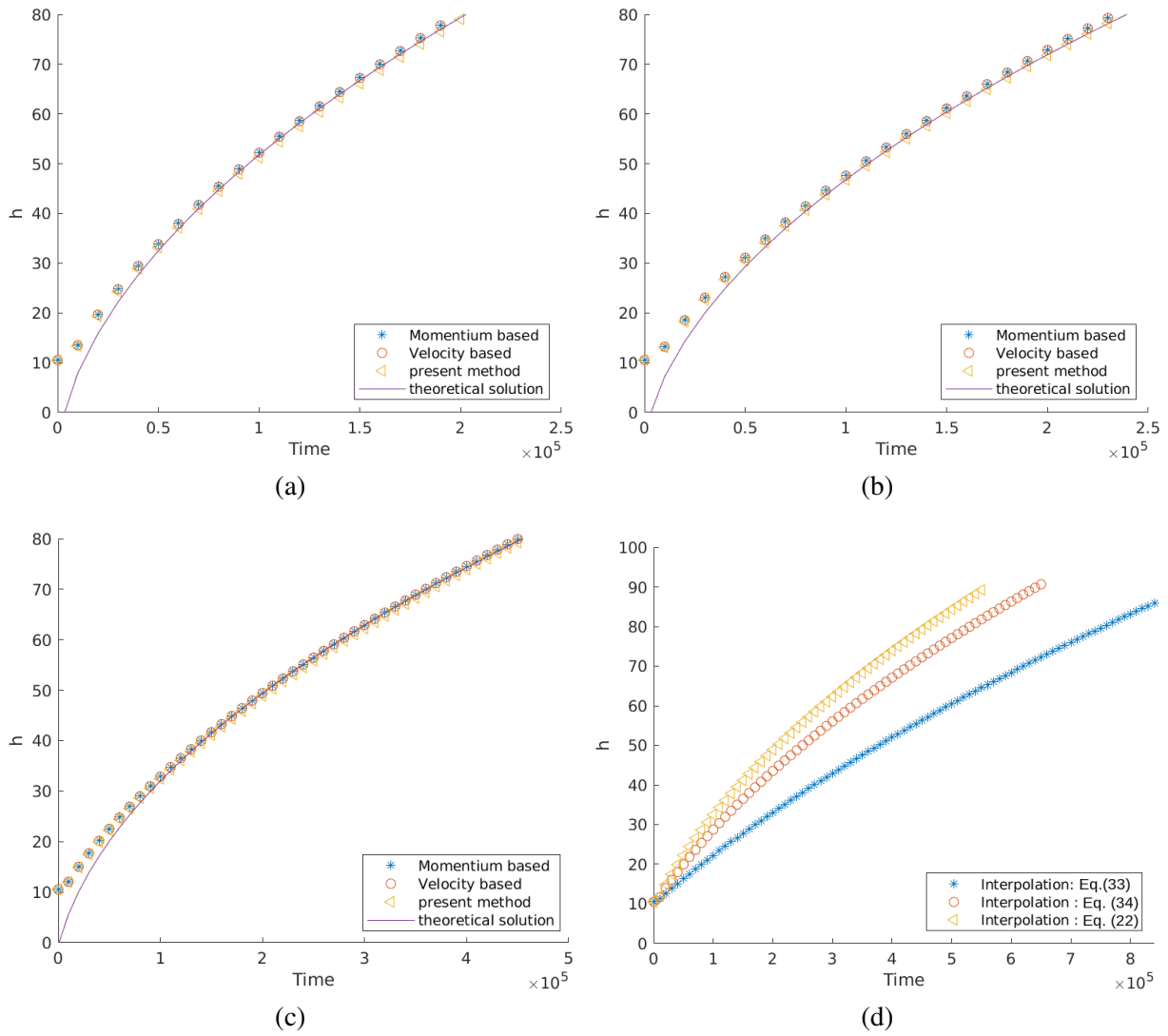


Fig. 15. (a)–(c) Comparison of the height of the meniscus in the cylindrical capillary between the numerical solutions and the theoretical solution (solid lines): (a)  $\theta = 30^\circ$ , (b)  $\theta = 45^\circ$ , (c)  $\theta = 70^\circ$ , and (d) effect of the relaxation time using different interpolation schemes

The results for the capillary flow using different methods for interpolation of dynamic viscosity (see Section 2.3.4) are shown in Fig. 15d. Both (33) and (34) yield an underestimation of the velocity. In Fig. 2, the dynamic viscosity across the phase interface is plotted for the three interpolation methods. It is clear that both (33) and (34) result in a region of high viscosity which extends into the low viscosity region ( $x > 0$ ). Especially using equation (33) results in a region with an artificially high viscosity, several times higher than the viscosity of the most viscous fluid, which implies, in agreement with (51), an underestimation of the liquid velocity.

#### 4. Conclusions

In this work, we propose a phase-field lattice Boltzmann model for simulation of immiscible fluids at high density ratios in three space dimensions. An accurate method has been proposed for prescribing the three-phase contact angle on curved boundaries and improvements have been made to the velocity-based model by Fakhari et al. [10] to achieve higher accuracy.

The first two test cases of droplets on flat and curved surfaces show the accuracy of the boundary conditions and the volume conservation of the model. Simulations are accurate at least in a range of contact angles from  $30^\circ$  to  $150^\circ$ . Outside this range the simulations are still stable, but there seems to be room for improvement on the boundary conditions for the phase-field equations. The simulations of flow between parallel plates show, as was known before, that the momentum-based model performs very badly at high density ratios. Additionally, we see improvements in accuracy using our model compared to the previous velocity-based model.

For the test case of a stationary meniscus, the moment-based method is most accurate in computing the pressure jump across the meniscus, and therefore yields the most stationary meniscus. While our proposed method improves the accuracy of the velocity-based model significantly, it is still not as accurate as the momentum-based method for this test case. Finally, for the dynamic capillary flow, the differences between the three methods are small and they all agree with theory after some time, provided a suitable dynamic contact angle is chosen.

In summary, our proposed method increases the accuracy of the computation of force terms and therefore improves the accuracy in all test cases compared to the previous velocity-based model [10]. The momentum-based model [9] performs well in simulating the stationary meniscus, but our results confirm that the proposed velocity-based method yields improved accuracy for layered flows and better consistency in dynamic capillary simulations. The proposed boundary conditions perform well for a wide range of contact angles on flat and curved boundaries. To conclude, our proposed method is a suitable method for high density ratio multi-phase flows in general geometries with improved accuracy compared to existing phase-field models.

Future work may include multiple relaxation time variants of the method, higher accuracy no-slip boundary conditions and investigation into more accurate boundary conditions for the phase-field for small contact angles. We will also apply the method to problems like multi-phase flow in porous media.

## References

- [1] Aihara, S., Takada, N., Takaki, T., Highly conservative Allen-Cahn-type multi-phase-field model and evaluation of its accuracy, *Theoretical and Computational Fluid Dynamics* 37 (2023) 639–659. <https://doi.org/10.1007/s00162-023-00655-0>
- [2] Ba, Y., Liu, H., Li, Q., Kang, Q., Sun, J., Multiple-relaxation-time color-gradient lattice Boltzmann model for simulating two-phase flows with high density ratio, *Physical Review E* 94 (2016) No. 023310. <https://doi.org/10.1103/PhysRevE.94.023310>
- [3] Bibette, J., Calderon, F. L., Poulin, P., Emulsions: Basic principles, *Reports on Progress in Physics* 62 (1999) 969–1033. <https://doi.org/10.1088/0034-4885/62/6/203>
- [4] Blunt, M. J., Flow in porous media – pore-network models and multiphase flow, *Current Opinion in Colloid & Interface Science* 6 (3) (2001) 197–207. [https://doi.org/10.1016/S1359-0294\(01\)00084-X](https://doi.org/10.1016/S1359-0294(01)00084-X)
- [5] Bracke, M., De Voeght, F., Joos, P., The kinetics of wetting: The dynamic contact angle, *Trends in Colloid and Interface Science III*, edited by Bothorel, P., Dufourc, E. J., Darmstadt, Steinkopff, 1989, pp. 142–149. <https://doi.org/10.1007/BFb0116200>
- [6] Brennen, C. E., *Fundamentals of multiphase flow*, Cambridge University Press, 2005. <https://doi.org/10.1017/CBO9780511807169>
- [7] d’Humières, D., Ginzburg, I., Krafczyk, M., Lallemand, P., Luo, L.-S., Multiple-relaxation-time lattice Boltzmann models in three dimensions, *Philosophical Transaction of the Royal Society A* 360 (2002) 437–451. <https://doi.org/10.1098/rsta.2001.0955>

- [8] Faghri, A., Zhang, Y., *Transport phenomena in multiphase systems*, Elsevier, 2006.
- [9] Fakhari, A., Bolster, D., Diffuse interface modeling of three-phase contact line dynamics on curved boundaries: A lattice Boltzmann model for large density and viscosity ratios, *Journal of Computational Physics* 334 (2017) 620–638. <https://doi.org/10.1016/J.JCP.2017.01.025>
- [10] Fakhari, A., Mitchell, T., Leonardi, C., Bolster, D., Improved locality of the phase-field lattice-Boltzmann model for immiscible fluids at high density ratios, *Physical Review E* 96 (2017) No. 053301. <https://doi.org/10.1103/PhysRevE.96.053301>
- [11] Geier, M., Schönherr, M., Pasquali, A., Krafczyk, M., The cumulant lattice Boltzmann equation in three dimensions: Theory and validation, *Computers & Mathematics with Applications* 70 (4) (2015) 507–547. <https://doi.org/10.1016/j.camwa.2015.05.001>
- [12] Gharibi, F., Ghavamnia, A., Ashrafizaadeh, M., Zhou, H., Thévenin, D., High viscosity ratio multicomponent flow simulations in porous media using a pseudo-potential central moment lattice Boltzmann method, *Chemical Engineering Science* 297 (2024) No. 120289. <https://doi.org/10.1016/j.ces.2024.120289>
- [13] Ginzburg, I., Generic boundary conditions for lattice Boltzmann models and their application to advection and anisotropic dispersion equations, *Advances in Water Resources* 28 (11) (2005) 1 196–1 216. <https://doi.org/10.1016/j.advwatres.2005.03.009>
- [14] Ginzburg, I., d’Humières, D., Multireflection boundary conditions for lattice Boltzmann models, *Physical Review E* 68 (2003) No. 066614. <https://doi.org/10.1103/PhysRevE.68.066614>
- [15] Guo, Z., Zheng, C., Shi, B., Discrete lattice effects on the forcing term in the lattice Boltzmann method, *Physical Review E* 65 (2002) No.046308. <https://doi.org/10.1103/PhysRevE.65.046308>
- [16] Günther, A., Jensen, K. F., *Multiphase microfluidics: From flow characteristics to chemical and materials synthesis*, *Lab on a Chip* 6 (2006) 1 487–1 503. <https://doi.org/10.1039/B609851G>
- [17] Han, C., *Multiphase flow in polymer processing*, Academic Press, 1981. <https://doi.org/10.1016/B978-0-12-322460-6.X5001-8>
- [18] He, X., Shan, X., Doolen, G. D., Discrete Boltzmann equation model for nonideal gases, *Physical Review E* 57 (1998) R13–R16. <https://doi.org/10.1103/PhysRevE.57.R13>
- [19] Hosseini, S. A., Atif, M., Ansumali, S., Karlin, I. V., Entropic lattice Boltzmann methods: A review, *Computers & Fluids* 259 (2023) No. 105884. <https://doi.org/10.1016/j.compfluid.2023.105884>
- [20] Jiang, T.-S., Oh, S.-G., Slattery, J. C., Correlation for dynamic contact angle, *Journal of Colloid and Interface Science* 69 (1) (1979) 74–77. [https://doi.org/10.1016/0021-9797\(79\)90081-X](https://doi.org/10.1016/0021-9797(79)90081-X)
- [21] Lafarge, T., Boivin, P., Odier, N., Cuenot, B., Improved color-gradient method for lattice Boltzmann modeling of two-phase flows, *Physics of Fluids* 33 (8) (2021) No. 082110. <https://doi.org/10.1063/5.0061638>
- [22] Lee, T., Liu, L., Lattice Boltzmann simulations of micron-scale drop impact on dry surfaces, *Journal of Computational Physics* 229 (20) (2010) 8 045–8 063. <http://doi.org/10.1016/j.jcp.2010.07.007>
- [23] Li, Q., Luo, K. H., Kang, Q. J., He, Y. L., Chen, Q., Liu, Q., Lattice Boltzmann methods for multiphase flow and phase-change heat transfer, *Progress in Energy and Combustion Science* 52 (2016) 62–105. <https://doi.org/10.1016/j.pecs.2015.10.001>
- [24] Li, Q., Xing, Y., Huang, R., Equations of state in multiphase lattice Boltzmann method revisited, *Physical Review E* 107 (2023) No. 015301. <https://doi.org/10.1103/PhysRevE.107.015301>
- [25] Liang, H., Xu, J., Chen, J., Wang, H., Chai, Z., Shi, B., Phase-field-based lattice Boltzmann modeling of large-density-ratio two-phase flows, *Physical Review E* 97 (2018) No. 033309. <https://doi.org/10.1103/PhysRevE.97.033309>

- [26] Liu, L., Lee, T., Wall free energy based polynomial boundary conditions for non-ideal gas lattice Boltzmann equation, *International Journal of Modern Physics C* 20 (11) (2009) 1 749–1 768. <https://doi.org/10.1142/s0129183109014710>
- [27] Liu, P., Zhao, J., Li, Z., Wang, H., Numerical simulation of multiphase multi-physics flow in underground reservoirs: Frontiers and challenges, *Capillarity* 12 (3) (2024) 72–79. <https://doi.org/10.46690/capi.2024.09.02>
- [28] Liu, Y., Feng, J., Min, J., Zhang, X., Homogenized color-gradient lattice Boltzmann model for immiscible two-phase flow in multiscale porous media, *Journal of Applied Physics* 135 (18) (2024) No. 184701. <https://doi.org/10.1063/5.0202947>
- [29] Masoodi, R., Pillai, K. M., Wicking in porous materials: Traditional and modern modeling approaches, Darmstadt, CRC Press, 2013. <https://doi.org/10.1201/b12972>
- [30] Mei, R., Luo, L.-S., Shyy, W., An accurate curved boundary treatment in the lattice Boltzmann method, *Journal of Computational Physics* 155 (2) (1999) 307–330. <https://doi.org/10.1006/jcph.1999.6334>
- [31] Otomo, H., Sun, C., Inamuro, T., Li, W., Dressler, M., Chen, H., Li, Y., Zhang, R., Lattice Boltzmann models for the hydrodynamic equations in multiphase flow with high density ratio, *Physics of Fluids* 37 (4) (2025) No. 043317. <https://doi.org/10.1063/5.0260829>
- [32] Peng, C., Ayala, L. F., Ayala, O. M., Wang, L.-P., Isotropy and spurious currents in pseudo-potential multiphase lattice Boltzmann models, *Computers & Fluids* 191 (2019) No. 104257. <https://doi.org/10.1016/j.compfluid.2019.104257>
- [33] Roccon, A., Zonta, F., Soldati, A., Phase-field modeling of complex interface dynamics in drop-laden turbulence, *Physical Review Fluids* 8 (2023) No. 090501. <https://doi.org/10.1103/PhysRevFluids.8.090501>
- [34] Seebergh, J. E., Berg, J. C., Dynamic wetting in the low capillary number regime, *Chemical Engineering Science* 47 (17–18) (1992) 4 455–4 464. [https://doi.org/10.1016/0009-2509\(92\)85123-5](https://doi.org/10.1016/0009-2509(92)85123-5)
- [35] Shao, J. Y., Shu, C., Huang, H. B., Chew, Y. T., Free-energy-based lattice Boltzmann model for the simulation of multiphase flows with density contrast, *Physical Review E* 89 (2014) No. 033309. <https://doi.org/10.1103/PhysRevE.89.033309>
- [36] Sharifi, R., Varmazyar, M., Mohammadi, A., Investigating droplet and bubble deformation under shear flow using the multi-pseudo-potential scheme of lattice Boltzmann method, *Advances in Applied Mathematics and Mechanics* 16 (2) (2024) 519–548. <https://doi.org/10.4208/aamm.OA-2021-0326>
- [37] Siebold, A., Nardin, M., Schultz, J., Walliser, A., Oppliger, M., Effect of dynamic contact angle on capillary rise phenomena, *Colloids and Surfaces A: Physicochemical and Engineering Aspects* 161 (1) (2000) 81–87. [https://doi.org/10.1016/S0927-7757\(99\)00327-1](https://doi.org/10.1016/S0927-7757(99)00327-1)
- [38] Stange, M., Dreyer, M. E., Rath, H. J., Capillary driven flow in circular cylindrical tubes, *Physics of Fluids* 15 (9) (2003) 2 587–2 601. <https://doi.org/10.1063/1.1596913>
- [39] Sukop, M.-C., Thorne, D. T., Lattice Boltzmann modeling: An introduction for geoscientists and engineers, Springer, 2007. <https://doi.org/10.1007/978-3-540-27982-2>
- [40] Sun, Y., Beckermann, C., Sharp interface tracking using the phase-field equation, *Journal of Computational Physics* 220 (2) (2007) 626–653. <https://doi.org/10.1016/j.jcp.2006.05.025>
- [41] Wang, L., He, K., Wang, H., Phase-field-based lattice Boltzmann model for simulating thermo-capillary flows, *Physical Review E* 108 (2023) No. 055306. <https://doi.org/10.1103/PhysRevE.108.055306>
- [42] Wu, J., Tan, Z., A conservative Allen-Cahn model for a hydrodynamics coupled phase-field sur-

factant system, *Mathematics and Computers in Simulation* 226 (2024) 42–65.  
<https://doi.org/10.1016/j.matcom.2024.06.016>

- [43] Zheng, L., Lee, T., Guo, Z., Rumschitzki, D., Shrinkage of bubbles and drops in the lattice Boltzmann equation method for nonideal gases, *Physical Review E* 89 (2014) No. 033302.  
<https://doi.org/10.1103/PhysRevE.89.033302>
- [44] Zhu, G., Chen, H., Li, A., Sun, S., Yao, J., Fully discrete energy stable scheme for a phase-field moving contact line model with variable densities and viscosities, *Applied Mathematical Modelling* 83 (2020) 614–639. <https://doi.org/10.1016/j.apm.2020.02.022>
- [45] Zu, Y. Q., He, S., Phase-field-based lattice Boltzmann model for incompressible binary fluid systems with density and viscosity contrasts, *Physical Review E* 87 (2013) No. 043301.  
<https://doi.org/10.1103/PhysRevE.87.043301>

## Appendix A – MRT scheme for the fluid

The multiple relaxation time (MRT) scheme used here is similar to the scheme presented in [10], but extended to three space dimensions. The collision operator

$$\Omega_q^{\text{SRT}} = -\frac{1}{\tau} (\bar{g}_q - \bar{g}_q^{eq}) \quad (54)$$

in (13) is replaced with the MRT counterpart

$$\Omega_q^{\text{MRT}} = -[M^{-1} \hat{S} M (\bar{g} - \bar{g}^{eq})]_q, \quad (55)$$

where  $\mathbf{g} = (g_0, \dots, g_{Q-1})^T$ . The matrix  $M$  is the transformation matrix into moment space, and  $\hat{S}$  is a diagonal matrix of reciprocal relaxation times. In this work, we have used the matrices for the D3Q19 model described by d’Humières et al. [7].

Additionally, the viscous force term  $F_\eta$  needs to be implemented differently in the MRT setting. Equation (18)<sub>2</sub> is therefore replaced by

$$F_{\eta,i}^{\text{MRT}} = -\frac{\nu}{c_s^2} \sum_{j=1}^d \left\{ \sum_{q=1}^Q e_{qi} e_{qj} [M^{-1} \hat{S} M (\bar{g} - \bar{g}^{eq})]_q \right\} \frac{\partial \varrho}{\partial x_j}, \quad (56)$$

where (20)–(22) are used to compute the required quantities.

## Appendix B – Units Conversion

In lattice Boltzmann (LBM) simulations, the mesh size and time step are commonly set to unity

$$\Delta x_{\text{LBM}} = 1 \text{ lu}, \quad \Delta t_{\text{LBM}} = 1 \text{ lu},$$

where ”lu” denotes lattice units. These differ from physical units (e.g., meters, seconds), and all LBM quantities must be rescaled accordingly to ensure consistency with the underlying physical model. We use the following convention: Physical quantities are marked with a tilde (e.g.,  $\tilde{x}$ ,  $\tilde{t}$ ,  $\tilde{\varrho}$ ), while lattice-based quantities are left unmarked. The conversions between physical and lattice units are defined as

$$\Delta x = C_L \tilde{x}, \quad \Delta t = C_t \tilde{t}, \quad \varrho = C_\varrho \tilde{\varrho},$$

where  $C_L$ ,  $C_t$ , and  $C_\rho$  are the unit conversion factors for length, time, and density, respectively. To determine the conversion of any derived physical quantity, one must express its SI units in terms of the base dimensions. For example, the surface tension  $\tilde{\sigma}$  has units

$$[\tilde{\sigma}] = \frac{\text{N}}{\text{m}} = \frac{\text{kg}}{\text{m} \cdot \text{s}^2} = \text{kg} \cdot \text{m}^{-1} \cdot \text{s}^{-2}.$$

Therefore, the relation between the physical and lattice surface tension becomes

$$\sigma = C_\rho \frac{C_L^3}{C_t^2} \tilde{\sigma}, \quad (57)$$

where  $\sigma$  is the surface tension in lattice units. This expression allows one to recover the physical surface tension from simulation parameters.